Received: 27 April 2023 | Revised: 4 January 2024 | Accepted: 7 February 2024

DOI: 10.1002/fld.5277

RESEARCH ARTICLE

WILEY

Predicting aerosol transmission in airplanes: Benefits of a joint approach using experiments and simulation

Christian Leithäuser[1] | **Victor Norrefeldt**[2] | **Elisa Thiel**[1] | **Michael Buschhaus**[2] | **Jörg Kuhnert**[1] | **Pratik Suchde**[1,3]

[1]Fraunhofer ITWM, Kaiserslautern, Germany

[2]Fraunhofer IBP, Valley, Germany

[3]University of Luxembourg, Esch-sur-Alzette, Luxembourg

Correspondence
Christian Leithäuser, Fraunhofer ITWM, Fraunhofer-Platz 1, 67663 Kaiserslautern, Germany.
Email: christian.leithaeuser@itwm.fraunhofer.de

Funding information
Horizon 2020 Framework Programme, Grant/Award Number: 892761; Bayerische Staatsministerium für Wirtschaft, Landesentwicklung und Energie, Grant/Award Number: ROB-2-3410.20_04-10-33/BLU-2109-0033; Fraunhofer-Gesellschaft: Fraunhofer vs. Corona

Summary

We investigate the transmission of aerosol particles in an airplane cabin with a joint approach using experiments and simulation. Experiments were conducted in a realistic aircraft cabin with heated dummies acting as passengers. A Sheffield head with an aerosol generator was used to emulate an infected passenger and particle numbers were measured at different locations throughout the cabin to quantify the exposure of other passengers. The same setting was simulated with a computational fluid dynamics model consisting of a Lagrange continuous phase for capturing the air flow, coupled with a Lagrange suspended discrete phase to represent the aerosols. Virtual measurements were derived from the simulation and compared with the experiments. Our main results are: the experimental setup provides good measurements well suited for model validation, the simulation does correctly reproduce the fundamental mechanisms of aerosol dispersion and simulations can help to improve the understanding of aerosol transmission for example by visualizing particle distributions. Furthermore, with findings from the simulation it was possible to crucially improve the experimental setup, proving that feedback between the numerical and the hardware world is indeed beneficial.

KEYWORDS

aerosol transmission, CFD, data analysis, meshfree, particulate matter, simulation

1 | INTRODUCTION

The modeling of aerosols is essential to understand the health and safety implications due to spread of bioaerosols such as viruses, bacteria and other airborne pathogens. This topic has received a lot of interest since the start of the COVID-19 pandemic. In efforts to mitigate the spread of the SARS-CoV-2 virus, a significant amount of research has been done to further the understanding of aerosol transmission. With a special focus on indoor environments, research in this direction has been used to estimate the appropriateness of different health and safety measures (e.g., Reference 1). Many experimental studies have been conducted to investigate particle transmission and the efficacy of face masks (e.g., References 2–5). To make faster predictions, various numerical simulation models have also been proposed. A lot of work has been done both from the perspective of general modeling of aerosol spread,[6–10] and for making predictions in specific

scenarios, ranging from hospital rooms,[11–13] classrooms[14] and restaurants,[15,16] to aircrafts,[17] cars[18] and buses.[19,20] We refer to References 21–23 for comprehensive reviews of different computational models for aerosol transmission. It is important to note that a majority of computational models for predicting aerosol transmission are not validated against experiments. This introduces significant uncertainties in applying these models to real world scenarios.

To overcome this, we choose a joint approach in the present work, where both simulations and experiments are carried out to study aerosol transmission in the same scenario, here inside an aircraft cabin. We introduce a Lagrange-Lagrange computational framework for modeling aerosol dispersion, and validate our model against our experimental results. Our study will demonstrate that the workflow to validate simulations by experimental data is not a one-way path, but that feedback between both the numerical and the hardware world is beneficial. We study the scenario of a fully occupied aircraft cabin where one passenger is assumed to be infected. Potentially virus-laden aerosol particles from this passenger are then traced throughout the cabin. Our experiments were carried out by Fraunhofer IBP at the Fraunhofer Flight Test Facility (FTF, see Reference 17) in Holzkirchen, Germany. Simulations of the same scenario were done by Fraunhofer ITWM using the in-house CFD software suite MESHFREE.[24] The potential applications of the present work, beyond virus-laden aerosols, also include various other physical phenoma concerning fine solid particles or liquid droplets suspended in air, ranging from the spread of air pollution[25] and pollen transmission,[26] to the impact of volcanic ash.[27]

Research on aerosol distribution in aircraft cabins, which are the application of the present study, has also been approached by the manufacturers themselves through different programs, like Airbus with the "Keep Trust in Air Travel" program, Boeing through the "Confident Travel Initiative", and Embraer through the "Healthy Journey" initiative. All these programs claim the cabin environment to be relatively safe due to HEPA filtration of recirculation air, a high air renewal rate, and a top-down airflow pattern. These analyses are based on the so-called perfect mixing assumption,[28] which neglects the spatial variation of aerosol concentration by assuming that air mixes to a homogeneous state in a very short period of time, typically 2 to 3 min. This same assumption has also been made to speed up simulation based approaches to model aerosol transmission in airplanes.[29] However, both measurements[30,31] and computational models[32,33] clearly show a spatial variation with increased concentrations closer to the emitter and lower concentrations farther away. Experimental work has even shown that the actual risk of infection can be higher than that predicted by the perfect mixing assumption.[34] Thus, in the simulations in the present work, we do not make the perfect mixing assumption and consider transient Lagrangian simulations to predict aerosol concentrations throughout the aircraft cabin.

The main results from our study are the following: The experimental approach in the controlled but realistic environment of the FTF leads to meaningful measurements which can be used to validate a simulation model. The fundamental mechanisms of aerosol dispersion are correctly reproduced by the model. Findings from the model observation can help to crucially improve the experimental setup. We also show how simulations can help to analyze and understand the key effects in aerosol dispersion for a specific scenario.

This study is structured in the following way: In Section 2, we begin by defining the two variations of the aircraft scenario which are investigated throughout the rest of the paper. The methods used in the experimental study, the numerical scheme and the simulation setup are introduced in Section 3. Experimental results, simulation results and the comparison of both are given and discussed in Section 4. The discussion is finalized with a collection of the important limitations of the current approach before we end with concluding remarks in Section 5.

2 | PRELIMINARIES

In this section, we briefly give an overview of the two scenarios considered in both experiments and simulations performed, and introduce the abbreviations used to refer to each scenario. A detailed explanation of the experimental setup and the simulation approach is presented in the next section.

The experimental setup consists of a realistic aircraft cabin (see Figure 1A) with mannequin dummies acting as passengers at every seat (see Figure 1B). Henceforth, the mannequin dummies are referred to simply as dummies for the sake of brevity. A schematic of the entire aircraft cabin used for the experiments is shown in Figure 2. As buoyancy of emitted heat from passengers is an important effect for the air flow field within the cabin, the dummies are heated during experiment. We observe that this has a significant influence on the results, and is the primary motivating factor behind the two scenarios considered.

(A) (B)

FIGURE 1 Overview of experimental setup at the Fraunhofer FTF: Front view of the empty cabin (left), and a rear view of the fully occupied cabin with mannequin dummies in yellow (right). (A) Empty aircraft cabin. (B) Fully occupied aircraft cabin. [Colour figure can be viewed at wileyonlinelibrary.com]

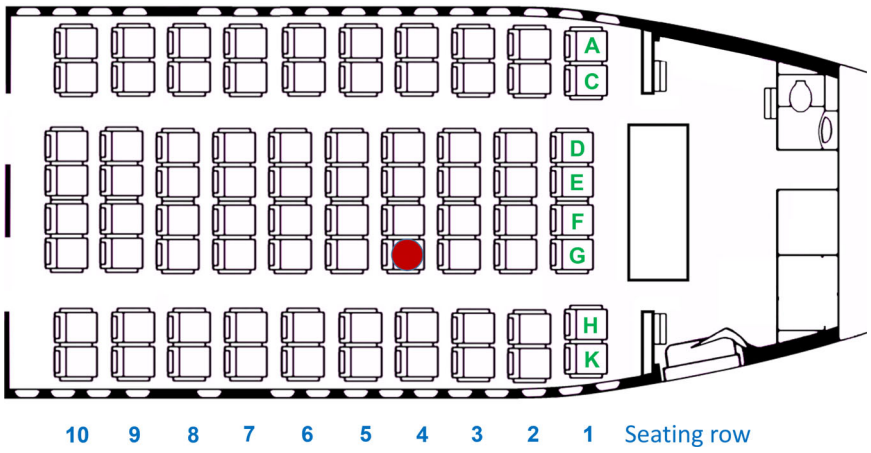

FIGURE 2 Schematic of the aircraft cabin used for the experimental setup. The seat numbers are marked in blue and green, indicating the row and column numbers respectively. The location of the infected passenger (4G) is marked in red. [Colour figure can be viewed at wileyonlinelibrary.com]

In all the experiments performed, we consider one infected passenger, located at seat 4G (see Figure 2). The infected passenger is represented by an aerosol generator connected to a Sheffield head (see Figures 3 and 4). In our first experiments, the source dummy at 4G was replaced with an aerosol generator without heating. In contrast to this, the first simulation model assumed all dummies to be heated, including the infected dummy. As a result, the simulation results did not agree with the experiment (more details in Section 4). We then turned off the heating of the source dummy at 4G in the simulations, which resulted in a good agreement between the simulation and experiment. This highlighted the importance of correctly modeling thermal and buoyant effects. We thus also considered a second scenario, where the experiment was repeated with a slightly modified setup in which the exhaled particles would directly enter the hot rising air stream of a heated dummy and the measurements changed as predicted by the original simulation where all dummies were heated.

The two previously described scenarios will be studied throughout the rest of the manuscript. We introduce the following shorthand to represent each of the scenarios concisely

- Scenario *Source4G_0W*: The source dummy (4G) is not heated. All other dummies are heated.
- Scenario *Source4G_75W*: All dummies are heated.

(A) (B)

FIGURE 3 Experimental setup in the Fraunhofer flight test facility (FTF) at Fraunhofer IBP: The "Sheffield head" aerosol generator (left) and the intake tubes for the measurement devices (right). (A) Particle source on seat 4G. (B) Particle measurement. [Colour figure can be viewed at wileyonlinelibrary.com]

(A) (B)

FIGURE 4 Setup of the aerosol source on seat 4G for the two scenarios considered: Neglecting heating at the source location (left), and with heating at the source location considered by repositioning the Sheffield head (right). In both scenarios, all other dummies are heated. The right figure also shows the particle source counters on a service trolley, that can be moved along the aircraft aisle. (A) Scenario *Source4G_0W*. (B) Scenario *Source4G_75W*. [Colour figure can be viewed at wileyonlinelibrary.com]

In both cases, the first part of the scenario name refers to the location of the aerosol source at seat 4G. The second part refers to the power used to heat the infected dummy.

3 | MATERIALS AND METHODS

In this section, we explain the experimental setup used in further detail, the computational models employed, and the simulation setup.

3.1 | Experimental setup

The experimental tests were conducted in the Fraunhofer Flight Test Facility (see, e.g., References 17,35,36), henceforth FTF, located in Holzkirchen, Germany. The FTF is a full-size demonstrator (see Figure 1) consisting of a front section of a long-range twin-aisle aircraft with a diameter of 9.6 m and a length of 30 m. It has a circulating air extraction in the triangle area (cheeks), corresponding exhaust air in the bilge section, and original ceiling air inlets. Furthermore, lateral air inlets have been refurbished to be compliant with aircraft cabins supplying air both below and above the stow bins. The cabin section consists of 10 rows of economy seating in a 2-4-2 arrangement, see Figure 2. The heat load and rough shape of passengers are represented by heated dummies (see Figures 3 and 4). These are Styrofoam bodies wrapped with a resistive wire, which emit 75 W each. Recirculation air is HEPA filter before being resupplied to the cabin ventilation. The ventilation was adjusted to a flow rate of 9.4l/s per passenger. The flow was divided to the ceiling air inlets (80%) and the lateral air inlets (20%). See Figure 5 for an illustration of the location of the air inlets.

A Sheffield head with an aerosol generator is placed on seat 4G within this setup. The aerosol generator (Figure 3A) is connected to a machine that ensures 9 breaths per minute at 0.715 l/breath airflow rate*. A Palas aerosol generator with a saline solution is placed below the head, thus providing aerosolized particles into the breathing flow. The aerosol generator is specified to emit particles in the diameter range from 5 nm to 15 μm.

Measurements of particle concentrations were carried out using two particle counters: A Fidas Frog particle counter with a measuring range of 0.18–20 μm and a WCPC particle counter with a measuring range of 2.5 nm–4 μm. Both particle counters are placed on a service trolley that is moved through the cabin. Measurements of particle concentrations were done at different seat numbers. At each measuring position, the sample inlet was fixed in the area of the heated dummy where the nose would be (Figure 3B). At each location, measurements were taken for 5 min before moving to the next location. Measurements are shown in Figures 6 and 7. These values are time averaged particle number concentrations (dCn) consecutively measured in the cabin.

Two series of tests were carried out on different days for our two scenarios. In the first test representing scenario *Source4G_0W* the heated dummy on seat 4G was removed and the Sheffield head with the aerosol generator was installed. This setup is shown in Figure 4A. In the second test representing scenario *Source4G_75W* the Sheffield head was reoriented on seat 4G such that it breaths into the plume produced by the heated dummy on seat 3G. Hence, particles could lift with the plume now. The setup for this scenario is shown in Figure 4B.

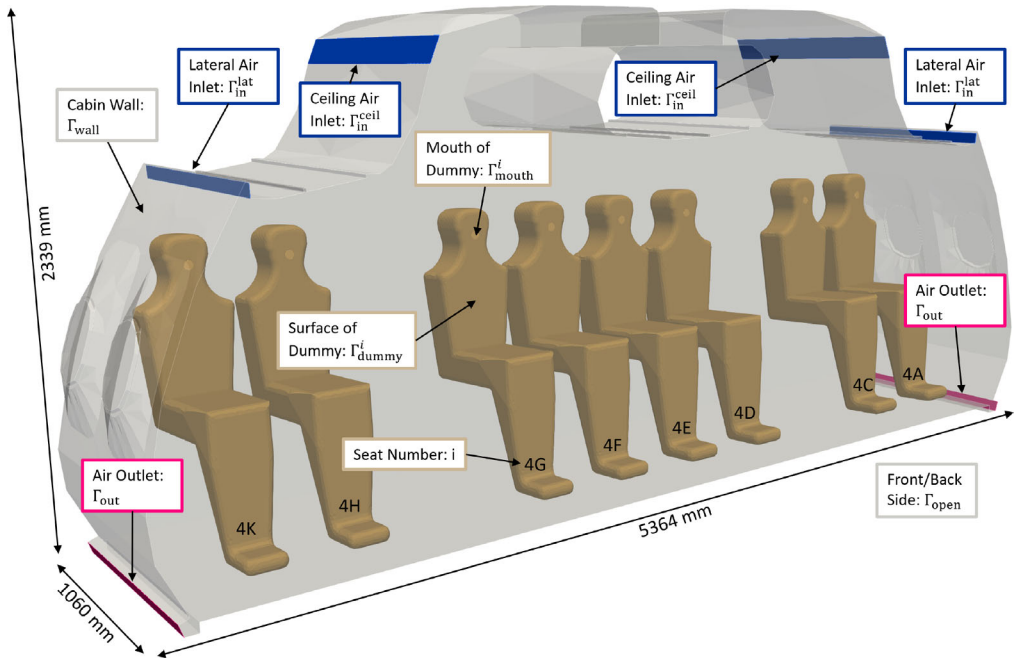

FIGURE 5 Computational geometry for the simulations. Only a single row of passengers is considered in the simulations, the implications of which are discussed in Section 4.4. The ceiling and lateral air inlets are marked in blue, while the air outlets at the floor are marked in pink. [Colour figure can be viewed at wileyonlinelibrary.com]

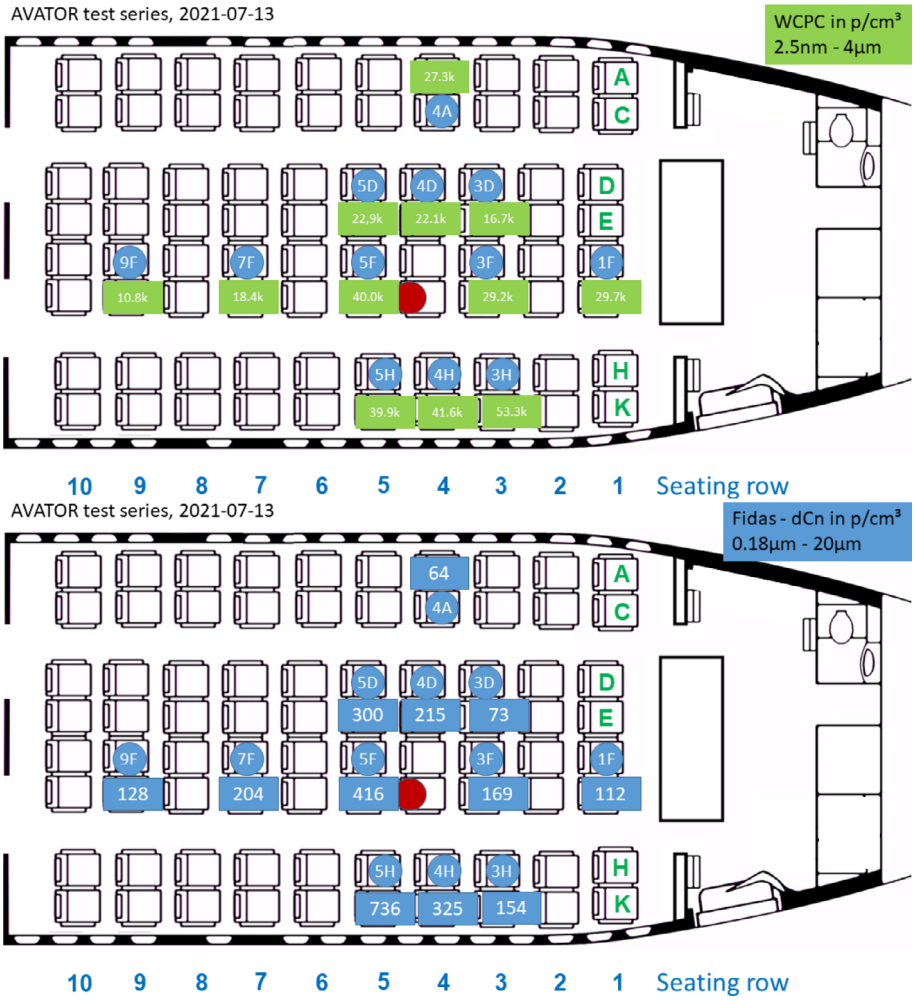

FIGURE 6 Measurements for scenario *Source4G_0W* carried out during the AVATOR project on July 13, 2021. The seat numbers where measurements were carried out are shown in blue circles. The corresponding concentrations measurements are shown beside the seat numbers. Concentrations measured by the WCPC particle counters are shown in green, and those by Fidas particle counter are shown in blue. [Colour figure can be viewed at wileyonlinelibrary.com]

3.2 | Computational modeling–Air phase

The computational modeling and simulations for both the air and droplet phases are done using the in-house software suite MESHFREE,[24] which is a very flexible multi-physics solver. The verification of the schemes, and validation of the basic numerical framework used can be found in our earlier work.[37–40]

The underlying mathematical model governing the simulations is a two phase flow process, comprising of a Lagrangian continuous phase for the air flow and a Lagrangian discrete phase for the aerosol. As the aerosol particles are very small, a one-way coupling of air flow to droplet phase is justified for modeling the aerosol spread in the simulated air flow. We explain the air phase modeling in the present subsection, and cover the aerosol modeling in the next subsection.

3.2.1 | Physical model

The physical model governing the air flow is given by the conservation of mass, momentum and energy equations in a Lagrangian formulation

$$\frac{D\rho}{Dt} = -\rho\nabla\cdot\vec{v}\,, \tag{1}$$

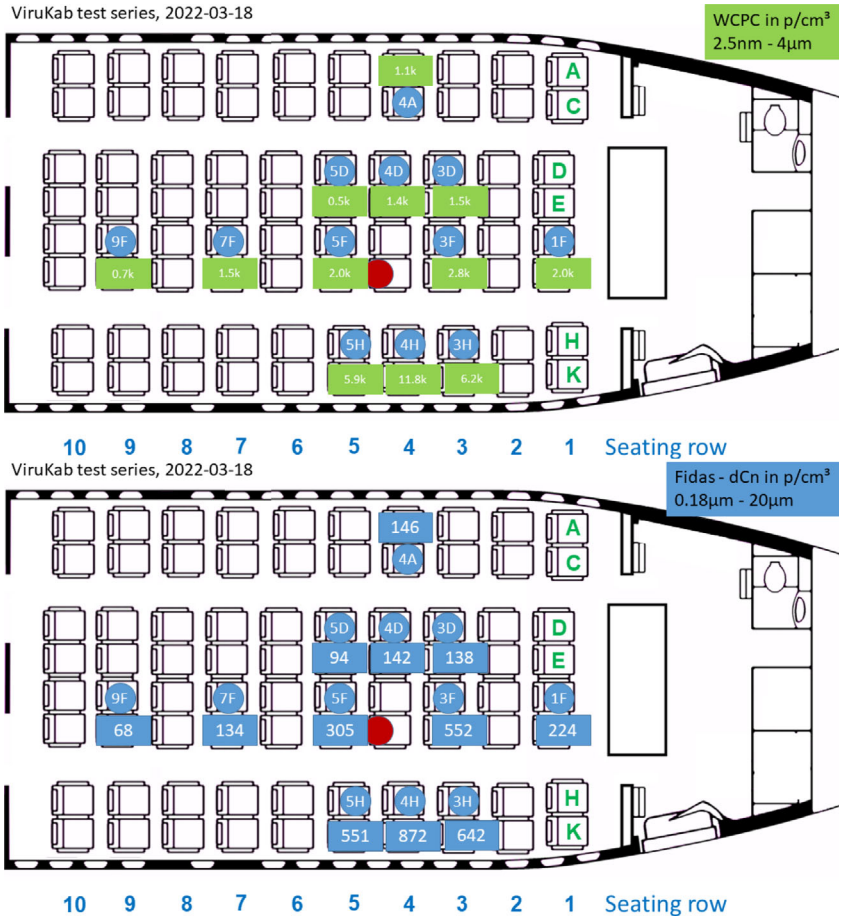

FIGURE 7 Measurements for scenario *Source4G_75W* carried out during the ViruKab project on March 18, 2022. The seat numbers where measurements were carried out are shown in blue circles. The corresponding concentrations measurements are shown beside the seat numbers. Concentrations measured by the WCPC particle counters are shown in green, and those by Fidas particle counter are shown in blue. [Colour figure can be viewed at wileyonlinelibrary.com]

$$\frac{D(\rho\vec{v})}{Dt} = \nabla \cdot \mathbf{S} - \nabla p + \rho\vec{g}\,, \tag{2}$$

$$\frac{D(\rho E)}{Dt} = \nabla \cdot (\mathbf{S}\vec{v}) - \nabla \cdot (p\vec{v}) + \rho\vec{g} \cdot \vec{v} + \nabla \cdot (\lambda \nabla T) + q\,, \tag{3}$$

with $E = c_p T + \frac{1}{2}\vec{v} \cdot \vec{v}$, and primary variables density ρ, velocity $\vec{v}$, pressure p and temperature T. Here, $\vec{g}$ consists of gravity and body forces, c_p is the specific heat capacity, λ is the heat conductivity, and q contains heat sources. $\frac{D}{Dt}$ indicates the material derivative. The stress tensor $\mathbf{S}$ is composed only of viscous terms, and is given by

$$\mathbf{S} = \mathbf{S}(\vec{v}) = \eta_{\text{eff}}\left((\nabla\vec{v}) + (\nabla\vec{v})^T - \frac{2}{3}\nabla \cdot \vec{v}\,\mathbf{I}\right), \tag{4}$$

where η_{eff} is the effective viscosity, consisting of a laminar part η and a turbulent part η_{turb}. The governing equations of Equations (1)–(3) are closed by the ideal gas law

$$\rho = \frac{p}{R_s T}, \tag{5}$$

where $R_s = 287.05\,\text{J/(kg K)}$ is the specific gas constant of air. Due to the ideal gas law, buoyancy is represented in the model. We also incorporate turbulent effects in the air flow with a standard k-ε turbulence model, with fluctuating dilatation and source terms omitted,[41,42] and a logarithmic wall function in the vicinity of wall boundaries.

To simplify the notation, we did not explicitly state that the variables in Equations (1)–(5) are for the air phase. Henceforth, physical properties and variables of the air phase are denoted with the subscript *air*, for example, $\vec{v}_{\text{air}}$, p_{air} and ρ_{air}.

3.2.2 | Meshfree point cloud formulation

To discretize the computational domain of the air phase, a *cloud* of scattered and unstructured points are placed on both the interior and the boundary of the domain.[43] This meshfree formulation of domain discretization is used to avoid the process of mesh generation in the complex domain within the airline cabin. Throughout the simulation, points move in a Lagrangian sense with the fluid velocity field. Thinning and filling procedures are employed to fix any resultant distortion that may arise.[39,43,44]

3.2.3 | Derivative computation

All spatial derivatives are approximated using a meshfree Generalized Finite Difference Method (GFDM),[45–48] which is a collocation method that generalizes classical finite differences to arbitrarily spaced points.[49,50] GFDMs have been widely shown to be robust, and have been used for a variety of applications, see, for example References 51–54.

3.2.4 | Time integration

The time integration begins with the Lagrangian motion of the points, which is done using an explicit second order method.[55] This is followed by the determination of the pressure and velocity using a segregated approach which resembles a Chorin-type projection method.[40,53,56] The next step is to update the temperature field with an implicit Euler integration of the energy conservation equation, followed by the numerical integration of the turbulent kinetic energy and disspiation.[51] For details of the overall numerical scheme, we refer to our earlier work.[38,51,53]

3.3 | Computational modeling–Aerosol phase

We model the aerosol with a finite number of particles or droplets suspended in the air flow. We henceforth use the nomenclature of *droplets* and *particles* interchangeably and with the same meaning. This highlights the fact that in a general case, these could represent both solid particles and liquid droplets. We use the subscript *drop* to denote droplets/particles, and distinguish their physical properties from the corresponding ones of the air phase.

3.3.1 | Physical model

Droplets are assumed to be in free flight. They are modeled in a moving Lagrangian framework, with their movement governed by equations of motion

$$\frac{D\vec{v}_{\text{drop}}}{Dt} = \frac{\vec{F}_D}{m_{\text{drop}}} + \frac{\vec{F}_p}{m_{\text{drop}}} + \vec{g}, \tag{6}$$

where $\vec{v}_{\text{drop}}$ and m_{drop} are the velocity and mass of the droplet respectively. Furthermore, $\vec{F}_D$ denotes the drag force on the droplet, $\vec{F}_p$ denotes the force due to pressure gradients in the airflow, and $\vec{g}$ is the gravitational acceleration. The drag force on the droplet is determined using a classical drag equation

$$\vec{F}_D = \frac{1}{2} C_D \rho_{\text{air}} A_{\text{drop}} \left(\vec{v}_{\text{air}} - \vec{v}_{\text{drop}}\right) \|\vec{v}_{\text{air}} - \vec{v}_{\text{drop}}\|, \tag{7}$$

for droplet cross sectional area A_{drop}, and drag coefficient C_D. Furthermore, $\vec{v}_{\text{air}}$ is the velocity of the air phase at the location of the droplet. The pressure gradient force is given by

$$\vec{F}_p = -\nabla p_{\text{air}} V_{\text{drop}}, \tag{8}$$

where ∇p_{air} is the pressure gradient of the air phase at the droplet location, and V_{drop} is the volume of the droplet. The droplet is assumed to be perfectly spherical with a diameter d_{drop}. Thus, Equation (6) becomes

$$\frac{D\vec{v}_{\text{drop}}}{Dt} = \frac{3}{4} C_D \frac{\rho_{\text{air}}}{\rho_{\text{drop}}} \frac{1}{d_{\text{drop}}} \left(\vec{v}_{\text{air}} - \vec{v}_{\text{drop}}\right) \|\vec{v}_{\text{air}} - \vec{v}_{\text{drop}}\| - \frac{1}{\rho_{\text{drop}}} \nabla p_{\text{air}} + \vec{g}, \tag{9}$$

with droplet density $\rho_{\text{drop}} = 10^3\ \text{kg/m}^3$.

3.3.2 | Time integration

Performing an explicit time integration of Equation (9) imposes a severe time step restriction. Explicit treatment of the drag term would restrict the time step used to a fraction of the particle relaxation time t_r given by

$$\frac{1}{t_r} = \frac{3}{4} C_D \frac{\rho_{\text{air}}}{\rho_{\text{drop}}} \frac{1}{d_{\text{drop}}} \|\vec{v}_{\text{air}} - \vec{v}_{\text{drop}}\|. \tag{10}$$

To avoid this time step restriction, we perform a semi-implicit time integration. We start by rewriting Equation (9) as

$$\frac{D\vec{v}_{\text{drop}}}{Dt} = \Phi\left(\vec{v}_{\text{air}} - \vec{v}_{\text{drop}}\right) + \vec{\Psi}, \tag{11}$$

where

$$\Phi = \frac{3}{4} C_D \frac{\rho_{\text{air}}}{\rho_{\text{drop}}} \frac{1}{d_{\text{drop}}} \|\vec{v}_{\text{air}} - \vec{v}_{\text{drop}}\|\ , \tag{12}$$

$$\vec{\Psi} = -\frac{1}{\rho_{\text{drop}}} \nabla p_{\text{air}} + \vec{g}\ . \tag{13}$$

For the time integration of Equation (11), we treat Φ explicitly, by assuming it to be constant within a time step. With this, we perform an analytical ODE integration of Equation (11) given by

$$\vec{v}_{\text{drop}}^{\,(n+1)} = \vec{K}^{\,(n)} + \left(\vec{v}_{\text{drop}}^{\,(n)} - \vec{K}^{\,(n)}\right) \exp(-\Delta t \Phi^{(n)}), \tag{14}$$

with

$$\vec{K}^{\,(n)} = \vec{v}_{\text{air}}^{\,(n)} + \frac{\vec{\Psi}^{(n)}}{\Phi^{(n)}}. \tag{15}$$

This velocity integration is preceded by the Lagrangian motion,[55] similar to that done for the air phase. The quantities stemming from the air phase, $\vec{v}_{\text{air}}$ and ∇p_{air}, are interpolated at the droplet positions from the corresponding values of nearby air phase points.

3.4 | Simulation setup

We now define the simulation setup for the air flow simulation and the subsequent droplet simulation. All relevant parameters used for the simulation are summarized in Table 1.

TABLE 1 Modeling parameters used in the simulations.

Parameter	Value	Description
V_{domain}	9.6 m^3	Volume of the computational domain
Air: Inlet boundary conditions on $\Gamma_{\text{in}}^{\text{ceil}}$ and $\Gamma_{\text{in}}^{\text{lat}}$		
N_{pass}	8	Number of passengers in the simulation domain
$\dot{V}_{\text{pass}}$	9.4l/s	Fresh air volume flow rate per passenger
f_{ceil}	80%	Fraction of total fresh air volume entering through $\Gamma_{\text{in}}^{\text{ceil}}$
f_{lat}	20%	Fraction of total fresh air volume entering through $\Gamma_{\text{in}}^{\text{lat}}$
T_{in}	16.4°C	Temperature of fresh air entering the cabin
Air: Boundary conditions on the surface of the heated dummies $\Gamma_{\text{dummy}}^{\text{i}}$		
$q_{\text{dummy}}^{\text{i}}$	75 W	Heat emitted by a single dummy *i* (except source dummy)
$q_{\text{dummy}}^{\text{4G}}$	0 W	Heat emitted by source dummy for scenario *Source4G_0W*
	75 W	Heat emitted by source dummy for scenario *Source4G_75W*
Air: Boundary conditions for the aerosol source $\Gamma_{\text{mouth}}^{\text{4G}}$		
$\dot{V}_{\text{breath}}$	0.715/breath	Volume of a single breath of the source dummy
f_{breath}	9 breath/min	Breath frequency of the source dummy
Air: Material parameters and initial conditions		
ρ_{air}	See ideal gas law Equation (5)	Temperature dependent density of air
λ_{air}	0.0262 W(m K)	Thermal conductivity of air
$c_{\text{p,air}}$	1000 J(kg K)	Specific heat capacity of air
η_{air}	0.00001 Pa s	Dynamic viscosity of air
T_{init}	23°C	Initial temperature of the air at the start of the simulation
Particles: Boundary conditions for the aerosol source		
	[5 nm, 15 μm]	Diameter range for the particles emitted by the source
	40	Number of discrete diameter species
	0.5 droplet/cm^3	Total particle concentration in the air emitted by the source
ρ_{drop}	1000 kg/cm^3	Density of aerosol droplet
Particles: Measurements		
	[2.5 nm, 4 μm]	Diameter detection range of the WCPC measurements
	[180 nm, 20 μm]	Diameter detection range of the Fidas measurements
r_{meas}	20 cm	Radius around face to evaluate simulated concentration

3.4.1 | Geometric setup

The computational domain for our simulation of the cabin scenario is shown in Figure 5. To keep the computational complexity in a feasible range, we restrict the domain to a single row of the cabin. This is a significant simplification, the implications of which will be discussed in Section 4.4. There are $N_{\text{pass}} = 8$ dummies within our domain which we identify by their seat number (4A, 4C, 4D, 4E, 4F, 4G, 4H and 4K). The dummy on seat 4G acts as the aerosol source and measurements are taken on seats 4A, 4D and 4H. Note that during the experiment tests at the FTF, measurements were also taken in other rows of the cabin. These are outside of our computational domain and can therefore not be used for the current comparison.

3.4.2 | Air flow simulation

Fresh air enters the cabin through the air inlets (see Figure 5). The volume flow rate is $\dot{V}_{\text{pass}} = 9.4\text{l/s}$ per passenger. So the total flow rate for the simulated segment is

$$\dot{V}_{\text{in}} = N_{\text{pass}} \cdot \dot{V}_{\text{pass}} = 75.2\text{l/s},$$

where $f_{\text{ceil}} = 80\%$ enter through the ceiling air inlets $\Gamma_{\text{in}}^{\text{ceil}}$ and $f_{\text{lat}} = 20\%$ through the lateral air inlets $\Gamma_{\text{in}}^{\text{lat}}$. The temperature of the fresh air is $T_{\text{in}} = 16.4°\text{C}$. The flow rate and temperature of the air inlets are chosen such that an average temperature of 23°C is maintained within the cabin, when considering the heat emitted by the passengers. The air outlet Γ_{out} is at the sides of the cabin floor. The boundary condition is such that the mass flow out of the domain matches the mass flow into the domain. Furthermore, the pressure is set to atmospheric pressure $p_0 = 1.01325 \times 10^5\text{Pa}$ at the outflow.

Each dummy i emits $q_{\text{dummy}}^{\text{i}} = 75$ W as a constant heat source uniformly distributed over the surface of the body. This is modeled by the boundary condition

$$\lambda_{\text{air}}\, \partial_n T = -\frac{q_{\text{dummy}}^{\text{i}}}{A_{\text{dummy}}^{\text{i}}} \qquad \text{on } \Gamma_{\text{dummy}}^{\text{i}} \tag{16}$$

where $A_{\text{dummy}}^{\text{i}}$ is the surface area of $\Gamma_{\text{dummy}}^{\text{i}}$.

In scenario *Source4G_0W*, the Sheffield head on seat 4G is acting as the aerosol source without internal heating (Figure 4A). For this setup the orange Styrofoam dummy was removed to make room for the aerosol generator. Thus the heat source on seat 4G is set to

$$q_{\text{dummy}}^{\text{4G}} = 0 \text{ W} \qquad \text{for scenario } \textit{Source4G\_0W}. \tag{17}$$

For scenario *Source4G_75W*, the heat source on 4G was set to

$$q_{\text{dummy}}^{\text{4G}} = 75 \text{ W} \qquad \text{for scenario } \textit{Source4G\_75W} \tag{18}$$

similar to all other dummies.

> *Remark* 1. For both simulation scenarios the same computational geometry (Figure 5) was used, that is, geometrically it was not accounted for whether the dummy on 4G was present or not. Instead the heat source term in the boundary condition of the dummy was turned off and on, respectively. Furthermore, we want to point out that in the experimental setup for scenario *Source4G_75W* the Sheffield head was repositioned so that it would breath into the plume of the dummy on 3G (Figure 4B). While we expect that this has a similar rising effect on the droplets, it is not the exact same setting as considered in the simulation.

The boundary condition $\Gamma_{\text{mouth}}^{\text{4G}}$ for the mouth of the source dummy is modeled with an alternating volume flow rate

$$\dot{V}_{\text{mouth}}^{4G}(t) = \dot{V}_{\text{breath}} f_{\text{breath}} \pi \sin(2\pi t f_{\text{breath}}) \tag{19}$$

where $\dot{V}_{\text{breath}} = 0.715l/\text{breath}$ is the volume of a single breath and $f_{\text{breath}} = 9\,\text{breath/ min}$ is the breath frequency while t is the simulation time. The exhale temperature of the artificial aerosol generator is assumed to be $T_{\text{breath}} = 23°\text{C}$. For the other dummies no breathing is modeled.

The cabin wall Γ_{wall} is modeled as an isolated no-slip wall. The front and back boundaries Γ_{open} of the computational domain, which are open to the rest of the cabin, are modeled as isolated slip walls.

An important aspect when modeling interior air flow is buoyancy, that is, warm air rises upwards. This especially happens in proximity to a body which heats the surrounding air. The reason for this effect is that the density of air changes with the temperature which is modeled by the ideal gas law Equation (5). The thermal conductivity $\lambda_{\text{air}} = 0.0262\ \text{W/(m K)}$ and specific heat capacity $c_{\text{p,air}} = 1000\,\text{J/(kg K)}$ of the air are assumed to be constant.

The simulation is initialized as a resting flow with a constant initial temperature of $T_{\text{init}} = 23°\text{C}$.

3.4.3 | Droplet simulation

The aerosol generator is specified to emit droplets in the diameter range from 5 nm to 15 μm. The exact diameter distribution and particle numbers are unknown and could not be measured because they exceeded the range of the sensors. For the simulation we use the following simple approach to sample droplets: We sample uniformly from 40 discrete diameters which are equally spaced in the logarithmic space in [5 nm, 15 μm]. For the simulation we use a representative droplet density of 0.5droplet/cm^3. In reality the droplet density is much larger so every simulated droplet represents many real droplets, but the absolute relation is unknown. The limitations of this rough estimate on the droplet distribution is discussed in Section 4.4.

We note that for simulating living passengers realistic aerosol concentrations can be found in Reference 57 and the protective effects of face masks can be modeled using loss curves from Reference 58.

3.4.4 | Evaluating particle measurements from simulation

The experiments used two instruments for the measurement of particle concentrations with different detection ranges:

- WCPC–Diameter detection range: [2.5 nm, 4 μm]
- Fidas–Diameter detection range: [180 nm, 20 μm]

We emulate taking virtual measurements from the simulation in the following way: Measurement positions within our computational domain are the seat positions 4A, 4D and 4H. At any given time during the simulation we evaluate the particle concentration within a ball of radius $r_{\text{meas}} = 20$ cm around the mouth of the dummy at the measurement position. Only the particles in the relevant diameter range (WCPC/Fidas) are considered when computing the concentration.

3.4.5 | Simulation sequence

The computational costs of the airflow simulation are the limiting factor for the computation. In total, 60 s of airflow were simulated. However, this is not enough to reach an equilibrium in the droplet simulation. Therefore the following strategy was used: The airflow was simulated for the time interval [0 s, 60 s]. Since the airflow was initialized with a resting flow we consider the first 20 s of the flow simulation as an initialization period. We assume that the interval [20 s, 60 s] is representative for the typical airflow in the cabin. Then, we start our droplet simulation at time 20 s and want to simulate for 480 s, that is, the simulation interval for the particle simulation is [20 s, 500 s]. The valid interval of the airflow simulation (i.e., [20 s, 60 s]) is periodically mapped to the droplet time. So this of course means that the airflow data which the particle simulation uses has a discontinuity every 40 s (e.g., at times 60 s, 100 s, …).

The particle simulation also needs some time to reach its equilibrium. The volume of our computational domain is $V_{\text{domain}} = 9.6$ m^3 and we can derive that between the start of the particle simulation and the time 300 s the air within the cabin has on average been exchanged 2.2 times by the ventilation system, and at time 500 s the air has been exchanged 3.8 times. For our analysis we will assume that this is enough to reach an equilibrium state and consider the interval [300 s, 500 s] as valid for taking measurements from the particle simulation (cf. Figures 9A and 10A).

4 | RESULTS AND DISCUSSION

We now summarize the results of the experiments and simulations, and provide a comparison of the two.

4.1 | Experimental results

Experiments were conducted on two separate days at the FTF. Measurements for scenario *Source4G_0W* were carried out on July 13, 2021 during the AVATOR[†] project. Since the simulation showed a major impact (cf. Figures 12 and

13) of the fact whether heating is provided below the Sheffield head, the test was repeated for scenario *Source4G_75W* to be more realistic of the actual airline cabin situation. The second test series was carried out on March 18, 2022 during the ViruKab[‡] project. A summary of the measurements recorded at different locations is given in Figures 6 and 7.

Since the tests were conducted on different dates, there is a possibility for uncontrolled changes in the test setup. Measurements were taken consecutively by moving the apparatus through the cabin. The supply airflow rates were monitored and it is assumed that the ventilation condition prevailed for the whole exposure so that the results are not expected to be influenced by temporal variations. The breathing apparatus releases particles as they are and there is no means to control the size distribution. It was tried to measure particle distribution directly in the breath, but concentrations exceeded the range of the sensors.

4.2 | Simulation results

A visualization of the simulation results for scenario *Source4G_0W* is shown in Figure 8. The air flow is shown in Figure 8A, with the color indicating the air velocity. The figure shows that air is moving upwards from the heated dummies. The source dummy on 4G is not heated for this scenario and the graphic shows less air movement in proximity to this dummy. Figure 8B shows the particle distribution shortly after the particle simulation was started and Figure 8C shows the particle distribution within the cabin after an equilibrium has been reached in the sense that local particle concentrations have leveled out.

Simulated particle concentrations relative to the source concentration for both scenarios are shown in Figures 9 and 10. The concentrations were determined from the simulations as described in Section 3.4 and then divided by the source concentration. Note that the relative concentration can be interpreted as the reduction factor between the concentration exhaled by the source and the concentration inhaled by another passenger. Figures 9A and 10A show the temporal evolution of the concentration. These plots were smoothed with a moving Gaussian average ($\sigma = 20\ s$). Figures 9B and 10B show bar plots of relative concentration averaged over the time interval [300 s, 500 s].

The simulated measurements are generally highest at seat 4H and lowest on the other side of the cabin at 4A. This is reasonable because the source at 4G is closer to 4H. The concentration at 4H is also higher than the concentration at 4D even though both positions have a similar distance to the source. This can be explained by the fact that the flow is roughly divided between the two sides of the cabin and more of the air which passes 4G tends to flow towards the air outlet at the floor near 4H.

Remarkable are the differences at seat 4H when comparing the two scenarios: In scenario *Source4G_75W* the concentration at 4H is about three times higher than in scenario *Source4G_0W*. The reason for these large differences may be understood from Figure 11: In scenario *Source4G_75W* the source dummy at 4G is heated and more air rises upwards in proximity to the source. The rising air also carries more particles upwards, as we can see from Figure 11A. These rising particles eventually reach the air flow from the ceiling inlets and are blown down in the direction of 4H (see Figure 11B). Of course a similar effect also happens in the unheated lab case *Source4G_0W*, but here less particles rise upwards so the effect is less prominent. Figure 11C compares the particle concentrations at the end of the simulations. The arrows illustrate the different main particle trajectories towards 4H which eventually lead to the surprisingly large differences in concentration between the two scenarios.

The differences between the diameter ranges of the WCPC (smaller) and Fidas (larger) particle counters do not seem to be significant at positions 4A and 4D. At position 4H there are less larger particles than smaller particles. A possible explanation might be the following: Many of the particles that reach 4H first move up from 4G to the ceiling and then drop down onto 4H. Here larger particles may have a disadvantage because they rise less easily. On the other hand, particles moving towards 4D and 4A cannot rise that high because the ceiling is blocked by the baggage compartments and thus their main trajectory is horizontal.

Computational costs for the simulations were significant: The air flow simulation (60 s of real time) took about 50 h on the Cluster "Beehive" of Fraunhofer ITWM using 168 cores (Intel Xeon Gold 6132 "Skylake" @ 2.6 GHz). The subsequent simulation of the aerosol particles (480 s of real time) took about 6 h. However, most of this time was spend on loading the air flow data from disk, leaving much room for improvement.

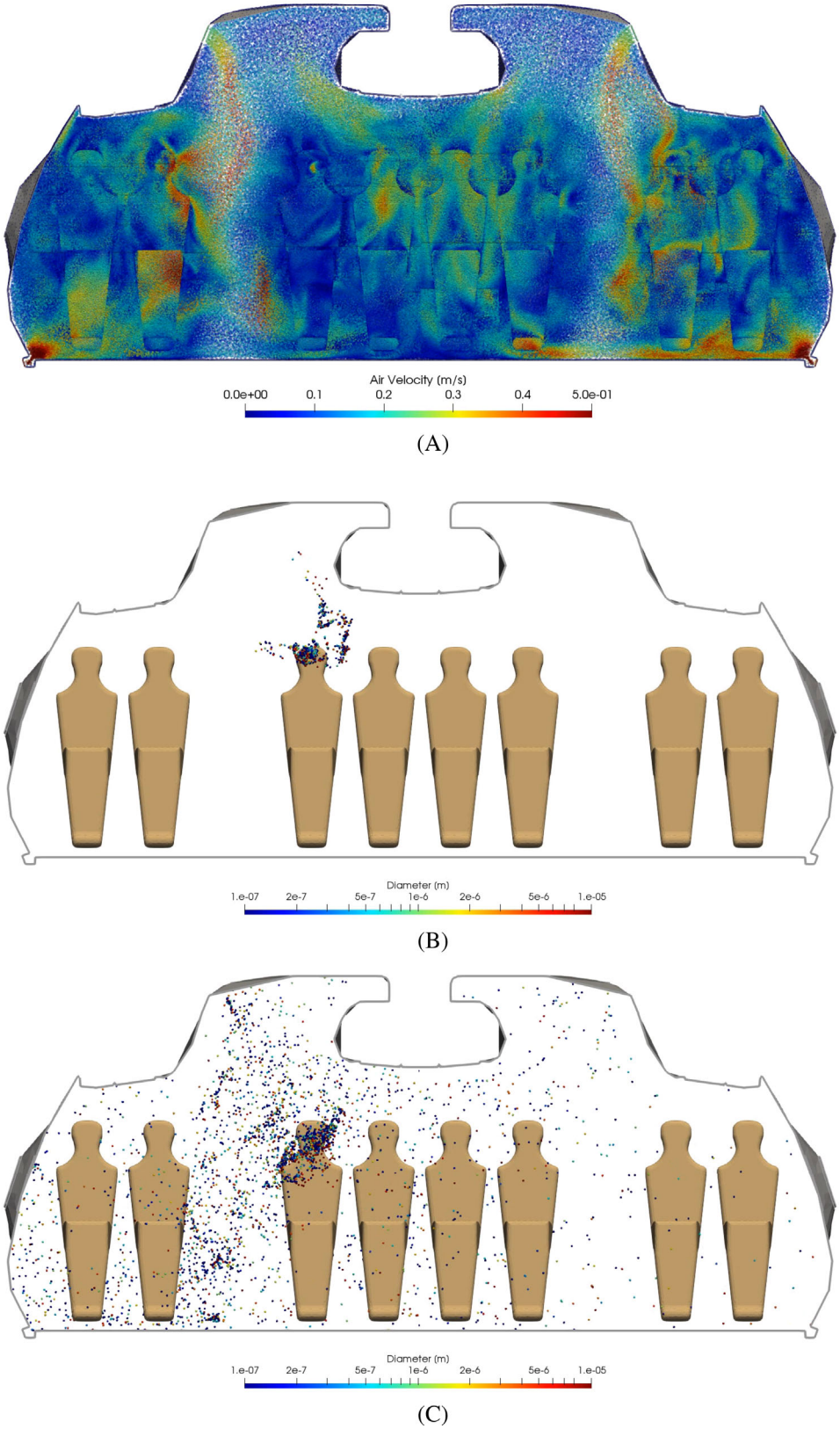

FIGURE 8 Visualization of the simulation results for scenario *Source4G_0W*. (A) Simulated airflow in the cabin. The color indicates the velocity. Note the slower air movement at the unheated source dummy on 4G. (B) Droplet distribution shortly after starting the droplet simulation. (C) Droplet distribution at the end of the simulation. [Colour figure can be viewed at wileyonlinelibrary.com]

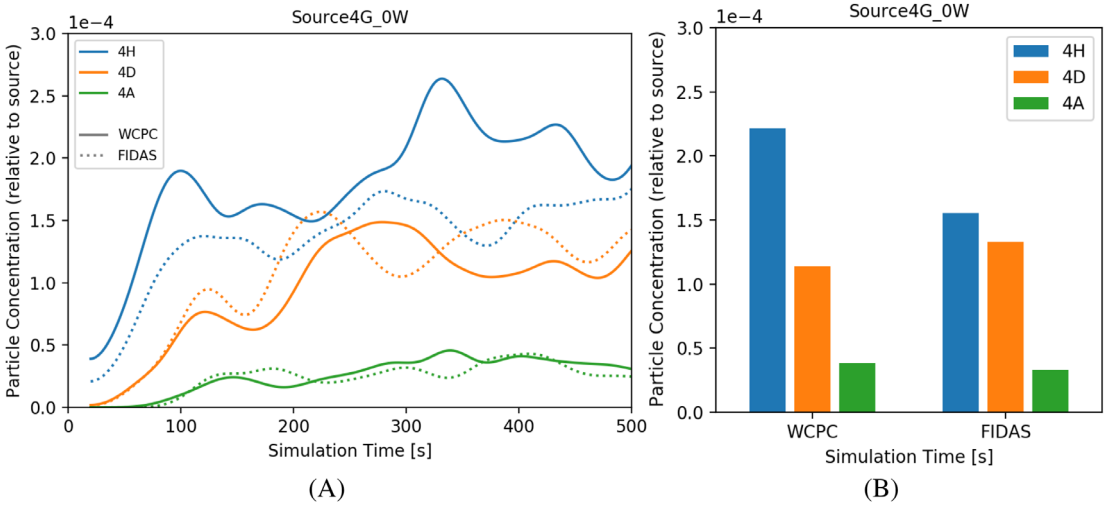

FIGURE 9 Simulation results: droplet concentration (relative to the source) for scenario *Source4G_0W*. Left: Time evolution of particle concentrations at different locations (seats 4H, 4D, 4A) and different particle size ranges (WCPC, Fidas). Right: Averaged concentration over the time interval [300 s, 500 s]. [Colour figure can be viewed at wileyonlinelibrary.com]

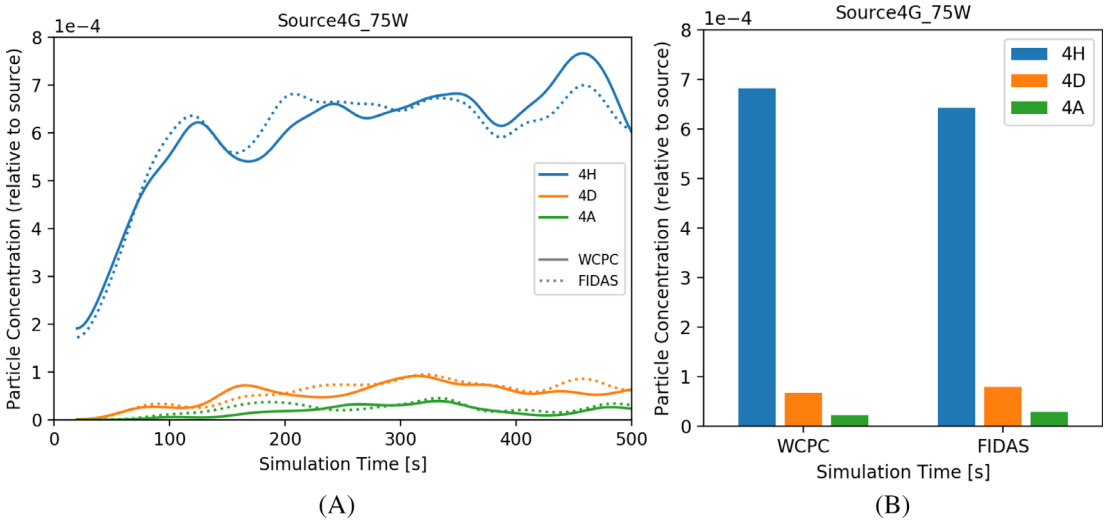

FIGURE 10 Simulation results: droplet concentration (relative to the source) for scenario *Source4G_75W*. Left: Time evolution of particle concentrations at different locations (seats 4H, 4D, 4A) and different particle size ranges (WCPC, Fidas). Right: Averaged concentration over the time interval [300 s, 500 s]. [Colour figure can be viewed at wileyonlinelibrary.com]

4.3 | Comparing simulation and experimental results

To keep the simulation costs in a feasible range the computational domain was limited to a single row of the aircraft cabin. Three of the measurement positions (4A, 4D, 4H) lie within this simulation domain and can be used for the comparison. However, the absolute particle concentration emitted by the aerosol generator is unknown and could not be measured because the concentration exceeded the measuring range of the sensors. Therefore, we can only compare relative concentrations. To do this we use position 4D as the reference: All measured concentrations are divided by the measured concentration at 4D and all simulated concentrations are divided by the simulated concentration at 4D. The resulting comparison of simulations against experimental measurements are shown in Figures 12 and 13.

The overall agreement between simulation and measurement is good. Especially the large differences in concentration at seat 4H between our two scenarios are confirmed by the experiments. At seat 4H, some deviations are obvious.

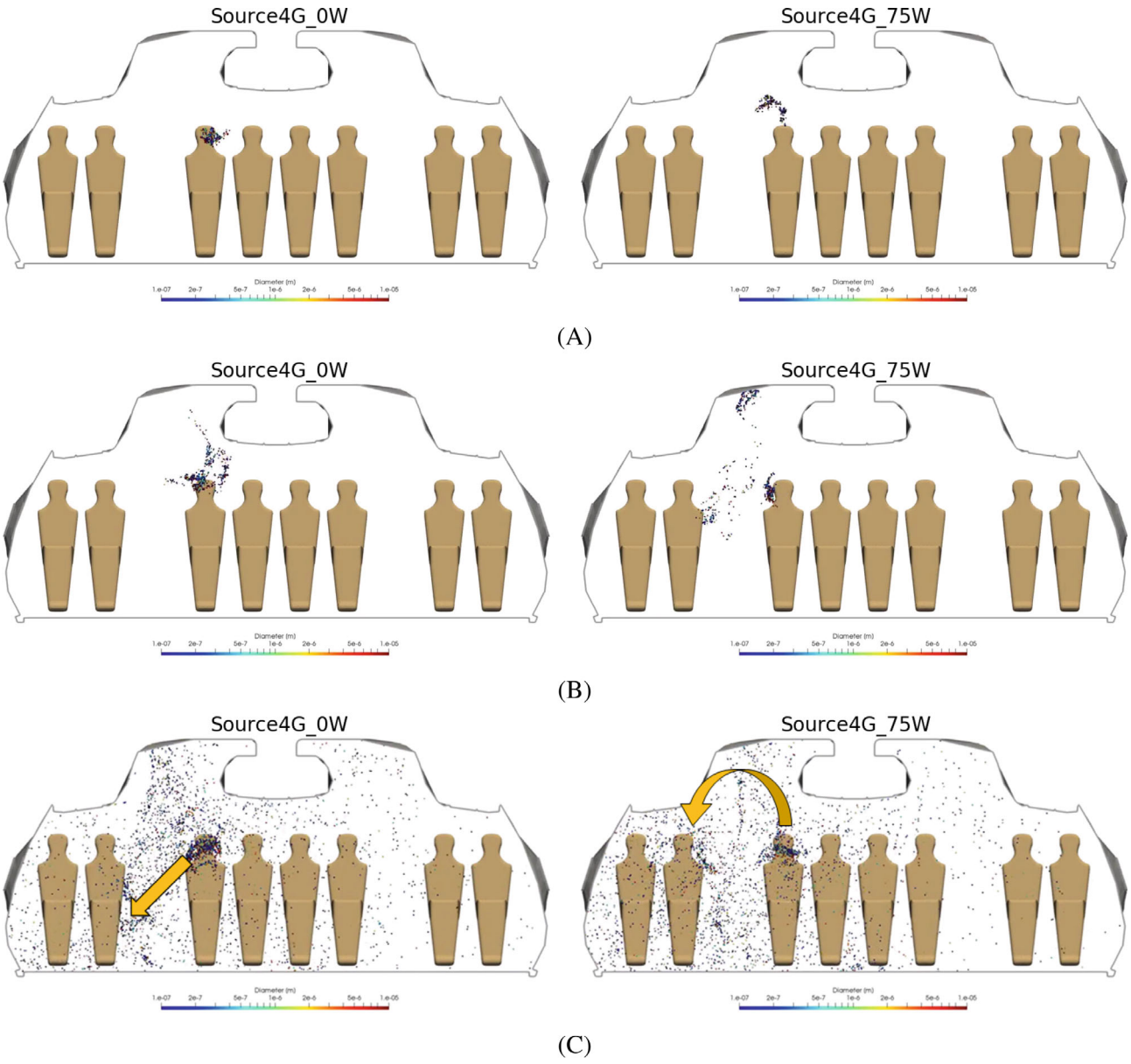

FIGURE 11 Comparison between the simulations of scenario *Source4G_0W* (left) and scenario *Source4G_75W* (right). (A) Immediately (3 s) after the start of the particle simulation. (B) Shortly (9 s) after the start of the particle simulation. (C) Equilibrium of the particle simulation. The arrow indicates the main particle trajectories from the source at 4G to the measurement location 4H. [Colour figure can be viewed at wileyonlinelibrary.com]

Measurement (Figures 6 and 7) reveals a high gradient between seats 3H, 4H and 5H. Hence, a small longitudinal variation will result in a relatively large change in particle concentration, thus being a challenge for 1:1 model validation.

In three of the four measurements at seat 4A the concentration is largely underestimated by the simulation. Potential cause can be simplifications used in the simulation model, like the rough estimate for the droplet size distribution which would have an impact on the particle drop rate. Since seat 4A is furthest away from the source a slightly larger drop rate could easily lead to a reduced particle accumulation at 4A. The cabin ventilation system has been implemented as symmetrically as possible, but an unbalance cannot be excluded that might lead to more particles being diverted towards seat 4A than expected by the fully symmetric setup assumed for the simulation.

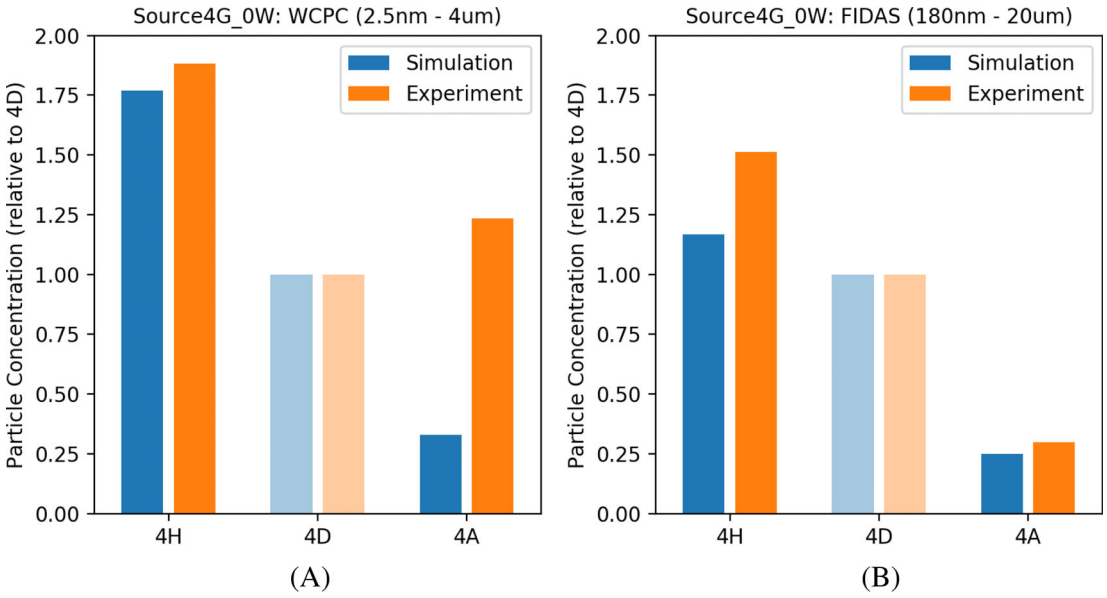

FIGURE 12 Comparison of simulations and experiments: Relative particle concentrations for scenario *Source4G_0W*. (A) WCPC (2.5 nm–4 μm). (B) Fidas (180 nm–20 μm). [Colour figure can be viewed at wileyonlinelibrary.com]

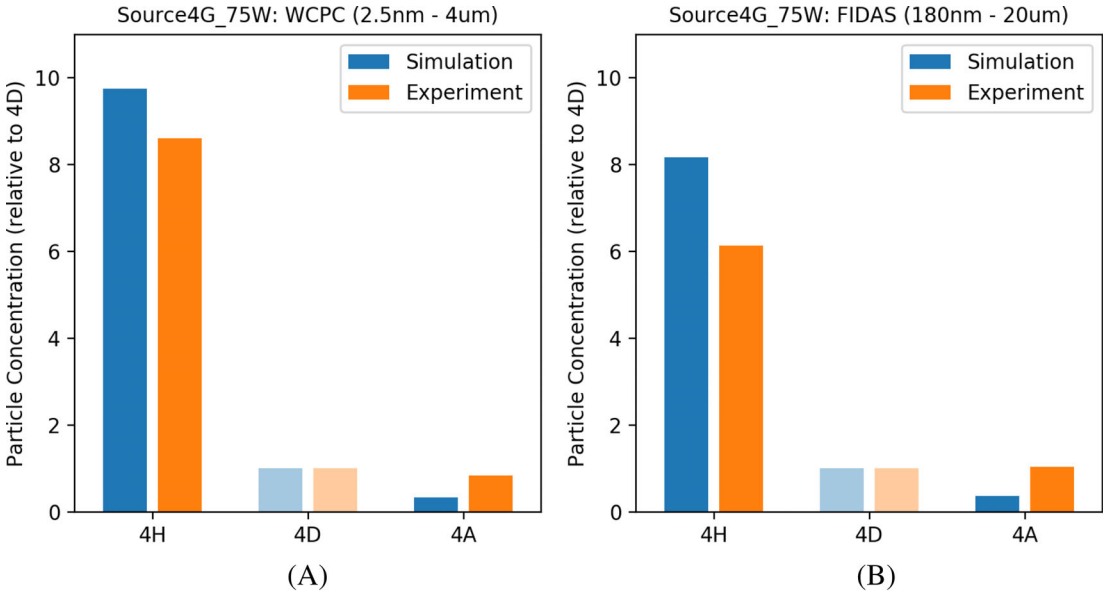

FIGURE 13 Comparison of simulations and experiments: Relative particle concentrations for scenario *Source4G_75W*. (A) WCPC (2.5 nm–4 μm). (B) Fidas (180 nm–20 μm). [Colour figure can be viewed at wileyonlinelibrary.com]

4.4 | Discussion of limitations

There are a number of limitations in the current approach which can be fixed to get more precise results: The computational domain for the simulation model is currently limited to one seating row. A larger domain would make more measurements available for comparison and it would reduce the influence of the open wall boundary conditions, thus improving the accuracy of the air flow simulation. The size of the computational domain is currently limited by the computational costs of the CFD simulation for the air flow. Another limitation is that the absolute number of particles released by the aerosol generator is unknown and could not be measured. As a result we had to use the measurement at 4D as a reference to compare experiment and simulation. Thus 4D could not be used as an independent measurement for

the validation. Overall, it would be very desirable to have more measurement positions which can be used for a proper validation of the simulations model. The logarithmically uniform distribution used by our model can certainly be refined by a better estimate or the exact distribution obtained from measurements. Another limitation was the setup of the aerosol source: For scenario *Source4G_75W* the Sheffield head was placed so that it would breath into the plume of the heated dummy sitting directly in front. We expect that this setup has a similar rising effect on the aerosol but it is not the exact same setting as a real passenger. It would be more realistic if the currently used Sheffield head and heated dummy could be combined into a single entity. Furthermore, the current scenarios are static with the Sheffield head always breathing in the same direction, in contrast to a real scenarios where passengers would move their heads and release aerosols in different directions.

5 | CONCLUSION

We presented a Lagrange-Lagrange computational model to predict aerosol dispersion inside airplanes using transient and non-isothermal flow. The simulation model is validated against experiments which were also done in the present study. This work shows that the workflow to validate simulations by experimental data is not a one-way path, but that feedback between both the numerical and the hardware world are beneficial. In a first attempt to validate the simulation against experimental data, the importance of the buoyancy induced airflow above passengers was clearly proven. As a result, the experiment was adjusted such that the breath interacted with a thermal plume of a dummy. This resulted in better match between simulation and experiment, due to a better suited test setup. Furthermore, measurements highlight the effect of distance from the emitter in the aircraft cabin. The cabin ventilation in combination with HEPA filtration proves to be effective on a global view, nevertheless sitting next to an infected passenger will result in increased levels of exposure.

AUTHOR CONTRIBUTIONS

Christian Leithäuser: Conceptualization, Formal Analysis, Funding Acquisition, Investigation, Project Administration, Validation, Writing – Original Draft, Writing – Review & Editing. **Victor Norrefeldt:** Conceptualization, Data Curation, Formal Analysis, Funding Acquisition, Investigation, Project Administration, Methodology, Writing – Review & Editing. **Elisa Thiel:** Conceptualization, Formal Analysis, Investigation, Software, Writing – Review & Editing. **Michael Buschhaus:** Data Curation, Formal Analysis, Investigation, Writing – Review & Editing. **Jörg Kuhnert:** Conceptualization, Funding Acquisition, Methodology, Software. **Pratik Suchde:** Methodology, Software, Writing – Original Draft, Writing – Review & Editing.

ACKNOWLEDGMENTS

All authors would like to acknowledge support from the Fraunhofer versus Corona campaign funded by the Fraunhofer Society under the project AVATOR. Research at Fraunhofer IBP was partly funded by the Bavarian Ministry of Economic Affairs, Regional Development and Energy, aviation research program BayLu25 under the project ViruKab, grant number ROB-2-3410.20_04-10-33/BLU-2109-0033. Pratik Suchde would also like to acknowledge partial support from the European Union's Horizon 2020 research and innovation programme under the Marie Skłodowska-Curie Actions grant agreement no. 892761 "SURFING". Open Access funding enabled and organized by Projekt DEAL.

CONFLICT OF INTEREST STATEMENT

The authors declare that there is no conflict of interest regarding the publication of this article.

DATA AVAILABILITY STATEMENT

Measurement data for the relevant experiments is comprehensively provided in Figures 6 and 7 within this article. The data that support the findings of this study are available from the corresponding author upon reasonable request.

ENDNOTES

*Fraunhofer IBP has filed a patent application for this setup with alternating aerosol generation.

†AVATOR–Anti-Virus-Aerosol: Testing, Operation, Reduction: Fraunhofer versus Corona campaign funded by Fraunhofer.

‡ViruKab: Aviation research program BayLu25 funded by the Bavarian Ministry of Economic Affairs.

ORCID

Christian Leithäuser https://orcid.org/0000-0001-8936-9805
Elisa Thiel https://orcid.org/0000-0003-2714-2861
Pratik Suchde https://orcid.org/0000-0002-4807-5322

REFERENCES

1. Bahl P, Doolan C, De Silva C, et al. Airborne or droplet precautions for health workers treating coronavirus disease 2019? *J Infect Dis*. 2022;225(9):1561-1568.
2. Ong SWX, Tan YK, Chia PY, et al. Air, surface environmental, and personal protective equipment contamination by severe acute respiratory syndrome coronavirus 2 (SARS-CoV-2) from a symptomatic patient. *Jama*. 2020;323(16):1610-1612.
3. Shah Y, Kurelek JW, Peterson SD, Yarusevych S. Experimental investigation of indoor aerosol dispersion and accumulation in the context of COVID-19: effects of masks and ventilation. *Phys Fluids*. 2021;33(7):073315.
4. Asadi S, Cappa CD, Barreda S, Wexler AS, Bouvier NM, Ristenpart WD. Efficacy of masks and face coverings in controlling outward aerosol particle emission from expiratory activities. *Sci Rep*. 2020;10(1):1-13.
5. Woodward H, de Kreij RJB, Kruger ES, et al. An evaluation of the risk of airborne transmission of COVID-19 on an inter-city train carriage. *Indoor Air*. 2022;32(10):e13121.
6. Buchan AG, Yang L, Atkinson KD. Predicting airborne coronavirus inactivation by far-uvc in populated rooms using a high-fidelity coupled radiation-CFD model. *Sci Rep*. 2020;10(1):1-7.
7. Dbouk T, Drikakis D. On coughing and airborne droplet transmission to humans. *Phys Fluids*. 2020;32(5):053310.
8. Fabregat A, Gisbert F, Vernet A, et al. Direct numerical simulation of turbulent dispersion of evaporative aerosol clouds produced by an intense expiratory event. *Phys Fluids*. 2021;33(3):033329.
9. Mariam AM, Joshi M, Rajagopal PS, Khan A, Rao MM, Sapra BK. CFD simulation of the airborne transmission of COVID-19 vectors emitted during respiratory mechanisms: revisiting the concept of safe distance. *ACS. Omega*. 2021;6(26):16876-16889.
10. Vuorinen V, Aarnio M, Alava M, et al. Modelling aerosol transport and virus exposure with numerical simulations in relation to SARS-CoV-2 transmission by inhalation indoors. *Safety Sci*. 2020;130:104866.
11. Crawford C, Vanoli E, Decorde B, et al. Modeling of aerosol transmission of airborne pathogens in ICU rooms of COVID-19 patients with acute respiratory failure. *Sci Rep*. 2021;11(1):1-12.
12. Leonard S, Strasser W, Whittle JS, et al. Reducing aerosol dispersion by high flow therapy in COVID-19: high resolution computational fluid dynamics simulations of particle behavior during high velocity nasal insufflation with a simple surgical mask. *J Am College Emerg Phys Open*. 2020;1(4):578-591.
13. Ren J, Duan S, Guo L, Li H, Kong X. Effects of return air inlets' location on the control of fine particle transportation in a simulated hospital ward. *Int J Environ Res Public Health*. 2022;19(18):11185.
14. Abuhegazy M, Talaat K, Anderoglu O, Poroseva SV. Numerical investigation of aerosol transport in a classroom with relevance to COVID-19. *Phys Fluids*. 2020;32(10):103311.
15. Liu H, He S, Shen L, Hong J. Simulation-based study of COVID-19 outbreak associated with air-conditioning in a restaurant. *Phys Fluids*. 2021;33(2):023301.
16. Oksanen L, Auvinen M, Kuula J, et al. Combining Phi6 as a surrogate virus and computational large-eddy simulations to study airborne transmission of SARS-CoV-2 in a restaurant. *Indoor Air*. 2022;32(11):e13165.
17. Schmohl A, Buschhaus M, Norrefeldt V, et al. Incremental evaluation model for the analysis of indoor air measurements. *Atmos*. 2022;13(10):1655.
18. Mathai V, Das A, Bailey JA, Breuer K. Airflows inside passenger cars and implications for airborne disease transmission. *Sci Adv*. 2021;7(1):eabe0166.
19. Zhang Z, Han T, Yoo KH, Capecelatro J, Boehman AL, Maki K. Disease transmission through expiratory aerosols on an urban bus. *Phys Fluids*. 2021;33(1):015116.
20. Yang Y, Wang Y, Tian L, Chuqi S, Chen Z, Huang Y. Effects of purifiers on the airborne transmission of droplets inside a bus. *Phys Fluids*. 2022;34(1):017108.
21. Katre P, Banerjee S, Balusamy S, Sahu KC. Fluid dynamics of respiratory droplets in the context of COVID-19: airborne and surfaceborne transmissions. *Phys Fluids*. 2021;33(8):081302.
22. Mohamadi F, Fazeli A. A review on applications of CFD modeling in COVID-19 pandemic. *Arch Comput Methods Eng*. 2022;29:3567-3586.
23. Zhao X, Liu S, Yin Y, Zhang T, Chen Q. Airborne transmission of COVID-19 virus in enclosed spaces: an overview of research methods. *Indoor Air*. 2022;32(6):e13056.
24. Fraunhofer Society. MESHFREE. https://www.meshfree.eu
25. Akimoto H. Global air quality and pollution. *Science*. 2003;302(5651):1716-1719.
26. Dbouk T, Drikakis D. On pollen and airborne virus transmission. *Phys Fluids*. 2021;33(6):063313.
27. Zhu Y, Toon OB, Jensen EJ, et al. Persisting volcanic ash particles impact stratospheric so2 lifetime and aerosol optical properties. *Nat Commun*. 2020;11(1):1-11.
28. Gupta JK, Lin C-H, Chen Q. Inhalation of expiratory droplets in aircraft cabins. *Indoor Air*. 2011;21(4):341-350.
29. Wang W, Wang F, Lai D, Chen Q. Evaluation of sars-cov-2 transmission and infection in airliner cabins. *Indoor Air*. 2022;32(1):e12979.

30. Silcott D, Kinahan S, Santarpia J, et al. *Transcom/Amc Commercial Aircraft Cabin Aerosol Dispersion Tests*. Technical report, Nebraska UnivZeteoTechS3i, LLC. National Strategic Research Inst; 2020.
31. Woodward H, Fan S, Bhagat RK, et al. Air flow experiments on a train carriage—towards understanding the risk of airborne transmission. *Atmos*. 2021;12(10):1267.
32. Matheis C, Norrefeldt V, Will H, et al. Modeling the airborne transmission of SARS-CoV-2 in public transport. *Atmos*. 2022;13(3):389.
33. Zee M, Davis AC, Clark AD, et al. Computational fluid dynamics modeling of cough transport in an aircraft cabin. *Sci Rep*. 2021;11(1):1-10.
34. Zhu S, Lin T, Laurent JGC, Spengler JD, Srebric J. Tradeoffs between ventilation, air mixing, and passenger density for the airborne transmission risk in airport transportation vehicles. *Build Environ*. 2022;219:109186.
35. Norrefeldt V, Mayer F, Herbig B, Ströhlein R, Wargocki P, Lei F. Effect of increased cabin recirculation airflow fraction on relative humidity, co2 and tvoc. *Aerospace*. 2021;8(1):15.
36. Herbig B, Norrefeldt V, Mayer F, Reichherzer A, Lei F, Wargocki P. Effects of increased recirculation air rate and aircraft cabin occupancy on passengers' health and well-being–results from a randomized controlled trial. *Environ Res*. 2022;216:114770.
37. Bender J. *Lagrangian-Lagrangian Fluid-Solid Coupling in a Generalized Finite Difference Framework*. PhD thesis. University of Kaiserslautern; 2020.
38. Drumm C, Tiwari S, Kuhnert J, Bart H-J. Finite pointset method for simulation of the liquid - liquid flow field in an extractor. *Comput Chem Eng*. 2008;32(12):2946-2957.
39. Seibold B. *M-Matrices in Meshless Finite Difference Methods*. PhD thesis. University of Kaiserslautern; 2006.
40. Suchde P, Kuhnert J, Tiwari S. On meshfree GFDM solvers for the incompressible Navier–Stokes equations. *Comput Fluids*. 2018;165:1-12.
41. Launder BE, Spalding DB. The numerical computation of turbulent flows. *Comput Methods Appl Mech Eng*. 1974;3(2):269-289.
42. Versteeg HK, Malalasekera W. *An Introduction to Computational Fluid Dynamics: the Finite volume method*. Pearson Education; 2007.
43. Suchde P, Jacquemin T, Davydov O. Point cloud generation for meshfree methods: an overview. *Arch Comput Methods Eng*. 2023;30:889-915.
44. Suchde P, Kuhnert J. A fully lagrangian meshfree framework for PDEs on evolving surfaces. *J Comput Phys*. 2019;395:38-59.
45. Suchde P, Kuhnert J. A meshfree generalized finite difference method for surface PDEs. *Comput Math Appl*. 2019;78(8):2789-2805.
46. Gavete L, Ureña F, Benito JJ, García A, Ureña M, Salete E. Solving second order non-linear elliptic partial differential equations using generalized finite difference method. *J Comput Appl Math*. 2017;318:378-387.
47. Fan C-M, Chu C-N, Šarler B, Li T-H. Numerical solutions of waves-current interactions by generalized finite difference method. *Eng Anal Bound Elem*. 2018;100:150-163.
48. Yu L, An-kang H, Liu Y-c. A finite pointset method for the numerical simulation of free surface flow around a ship. *J Marine Sci Technol*. 2016;21(2):190-202.
49. Liszka T, Orkisz J. The finite difference method at arbitrary irregular grids and its application in applied mechanics. *Comput Struct*. 1980;11(1-2):83-95.
50. Jacquemin T, Tomar S, Agathos K, Mohseni-Mofidi S, Bordas S. Taylor-series expansion based numerical methods: a primer, performance benchmarking and new approaches for problems with non-smooth solutions. *Arch Comput Methods Eng*. 2019;27:1465-1513.
51. Michel I, Seifarth T, Kuhnert J, Suchde P. A meshfree generalized finite difference method for solution mining processes. *Comput Particle Mech*. 2021;8(3):561-574.
52. Möller A, Kuhnert J. Simulation of the glass flow inside a floating process / simulation de l'écoulement du verre dans le procédé float. *Revue Verre*. 2007;13(5):28-30.
53. Jefferies A, Kuhnert J, Aschenbrenner L, Giffhorn U. Finite pointset method for the simulation of a vehicle travelling through a body of water. In: Griebel M, Schweitzer AM, eds. *Meshfree Methods for Partial Differential Equations VII*. Springer International Publishing; 2015:205-221.
54. Tramecon A, Kuhnert J. Simulation of advanced folded airbags with VPS-PAMCRASH/FPM: development and validation of turbulent flow numerical simulation techniques applied to curtain bag deployments. *SAE Technical Paper*. SAE International; 2013.
55. Suchde P, Kuhnert J. Point cloud movement for fully lagrangian meshfree methods. *J Comput Appl Math*. 2018;340:89-100.
56. Chorin AJ. Numerical solution of the navier-stokes equations. *Math Comput*. 1968;22(104):745-762.
57. Pöhlker ML, Krüger OO, Förster J-D, et al. Respiratory aerosols and droplets in the transmission of infectious diseases. arXiv preprint arXiv:2103.01188; 2021.
58. Grinshpun SA, Haruta H, Eninger RM, Reponen T, McKay RT, Lee S-A. Performance of an N95 filtering facepiece particulate respirator and a surgical mask during human breathing: two pathways for particle penetration. *J Occup Environ Hyg*. 2009;6(10):593-603.

How to cite this article: Leithäuser C, Norrefeldt V, Thiel E, Buschhaus M, Kuhnert J, Suchde P. Predicting aerosol transmission in airplanes: Benefits of a joint approach using experiments and simulation. *Int J Numer Meth Fluids*. 2024;96(6):991-1010. doi: 10.1002/fld.5277